1 **Spatial variations of effective elastic thickness of the lithosphere in**

2 **Central America and surrounding regions**

3

4 Alberto Jiménez-Díaz [a, b,*], Javier Ruiz [a], Marta Pérez-Gussinyé [c], Jon F. Kirby [d],

5 José A. Álvarez-Gómez [a], Rosa Tejero [a, b], Ramón Capote [a]

6

7 [a] Departamento de Geodinámica, Facultad de Ciencias Geológicas, Universidad

8 Complutense de Madrid. 28040 Madrid, Spain.

9 [b] Instituto de Geociencias, IGEO (CSIC, UCM). 28040 Madrid, Spain.

10 [c] Department of Earth Sciences, Royal Holloway, University of London, Egham Hill,

11 TW20 0EX Egham, United Kingdom.

12 [d] Department of Spatial Sciences, Curtin University, GPO Box U1987, Perth WA 6845,

13 Australia.

14

15

16 * Corresponding author:

17 Alberto Jiménez-Díaz

18 Departamento de Geodinámica, Facultad de CC. Geológicas,

19 Universidad Complutense de Madrid.

20 c/ José Antonio Nováis, 2. 28040 Madrid (Spain)

21 Tel: +34 91 394 4821; Fax: +34 91 394 4631.

22 E-mail address: ajimenezdiaz@geo.ucm.es

23

24

1   **Abstract**

2       As a proxy for long-term lithospheric strength, the effective elastic thickness ($T_e$)

3   can be used to understand the relationship between lithospheric rheology and

4   geodynamic evolution of complex tectonic settings. Here we present, for the first time,

5   high-resolution maps of spatial variations of $T_e$ in Central America and surrounding

6   regions from the analysis of the coherence between topography and Bouguer gravity

7   anomaly using multitaper and wavelet methods. Regardless of the technical differences

8   between the two methods, there is a good overall agreement in the spatial variations of

9   $T_e$ recovered from both methods. Although absolute $T_e$ values can vary in both maps,

10  the qualitative $T_e$ structure and location of the main $T_e$ gradients are very similar. The

11  pattern of the $T_e$ variations in Central America and surrounding regions agrees well with

12  the tectonic provinces in the region, and it is closely related to major tectonic

13  boundaries, where the Middle American and Lesser Antilles subduction zones are

14  characterized by a band of high $T_e$ on the downgoing slab seaward of the trenches.

15  These high $T_e$ values are related to internal loads (and in the case of the southernmost

16  tip of the Lesser Antilles subduction zone also associated with a large amount of

17  sediments) and should be interpreted with caution. Finally, there is a relatively good

18  correlation, despite some uncertainties, between surface heat flow and our $T_e$ results for

19  the study area. These results suggest that although this area is geologically complex, the

20  thermal state of the lithosphere has profound influence on its strength, such that $T_e$ is

21  strongly governed by thermal structure.

22

1    **1. Introduction**

2        The knowledge of lateral variations in lithosphere strength can aid in

3    understanding how surface deformation relates to deep Earth processes. As a proxy for

4    long-term lithospheric strength, the effective elastic thickness of the lithosphere ($T_e$)

5    corresponds to the thickness of an idealized elastic plate bending under the same applied

6    loads (Watts, 2001), and is related to the integrated mechanical strength of the

7    lithosphere (Burov and Diament, 1995). The knowledge of $T_e$ in different places

8    provides a measurement of the spatial variation of the lithospheric strength, which is

9    strongly controlled by local and regional conditions. Although $T_e$ does not represent an

10   actual depth to the base of the mechanical lithosphere, its spatial variations reflect

11   relative lateral variations in lithospheric mechanical thickness (see McNutt, 1984). Thus

12   it can be used to understand the relationship between lithospheric rheology and

13   geodynamic evolution of complex tectonic settings.

14       $T_e$ primarily depends on the thickness and structure of the crust, the composition

15   of the crust and the lithospheric mantle, the degree of their coupling, the thermal state of

16   the lithosphere, the state of stress, plate curvature, and the presence of melts, fluids and

17   faults (e.g., Lowry and Smith, 1995; Burov and Diament, 1995; Lowry et al., 2000;

18   Watts, 2001; Artemieva, 2011). The oceanic lithosphere generally behaves like a single

19   mechanical layer due to the thin crust, which is usually coupled to the lithospheric

20   mantle, and $T_e$ is to first order controlled by the thermal age of the lithosphere at the

21   time of loading (Watts, 2001; Kalnins and Watts, 2009). By contrast, the thermal state

22   and rheological behaviour of the lithosphere in continental areas are largely a

23   consequence of local conditions (e.g., Ranalli, 1997; Afonso and Ranalli, 2004;

24   Bürgmann and Dresen, 2008; Hasterok and Chapman, 2011; Mareschal and Jaupart,

1  2013), such that there is a complex relationship between $T_e$ and its controlling

2  parameters (Watts and Burov, 2003; Burov and Watts, 2006; Burov, 2011).

3    In this study we present, for the first time, high-resolution maps of spatial

4  variations of $T_e$ in Central America and surrounding regions from the analysis of the

5  Bouguer coherence using both multitaper and wavelet methods. The Central America-

6  Caribbean region is characterized by the interaction of six lithospheric plates (Fig. 1).

7  The Caribbean plate moves eastward relative to its two neighboring plates, North and

8  South America plates (DeMets et al., 2010), and its perimeter is characterized by a high

9  variability and complexity of geodynamic and tectonic processes (e.g., Sykes et al.,

10  1982; Ross and Scotese, 1988). Therefore, this area represents a good natural laboratory

11  to study the spatial variations of $T_e$, test the response of spectral methods to different

12  factors and geodynamic conditions, and examine relationships between surface

13  deformation, lithospheric structure and mantle dynamics.

14    In the following sections we first introduce the methodology and data employed

15  for estimating $T_e$. We then present our results and compare them to previous estimates

16  of $T_e$ in the study area. Finally, we examine the relationships between $T_e$ with other

17  proxies for lithospheric and sub-lithospheric structure to improve our knowledge of the

18  long-term rheology and mechanical behaviour of the lithosphere in the study area. We

19  also discuss how the lithospheric structure derived from our $T_e$ analysis relates to

20  surface deformation.

21

22  **2. $T_e$ estimation by spectral methods**

23    To estimate the effective elastic thickness we calculate the coherence function

24  relating the topography and Bouguer anomaly, commonly known as Bouguer

coherence, using multitaper and wavelet methods. This function gives information on the wavelength band over which topography and Bouguer anomaly are correlated. In the coherence deconvolution method of Forsyth (1985), $T_e$ is estimated by comparing the observed coherence curve with coherence functions predicted for a range of $T_e$ values. For each given $T_e$, we calculate via deconvolution the initial surface and subsurface loads and compensating deflections that generate a predicted topography and gravity that best fit the observed topography and gravity anomaly, and a predicted coherence that best fits the observed coherence (Forsyth, 1985). The $T_e$ value that minimizes the differences between the predicted and observed quantities is the optimal one for the analysed area. The Bouguer coherence generally tends to zero at short wavelengths, where the topography is not compensated and loads are supported predominantly by the elastic strength of the lithosphere (Forsyth, 1985). At long wavelengths, the response to loading approaches the Airy limit and the coherence tends to one. The wavelengths at which the coherence rapidly increases from 0 to 1 depend on the effective elastic thickness of the lithosphere, such that when the lithosphere is weak and $T_e$ is small, local compensation for loading occurs at relatively shorter wavelengths and vice versa.

In this Section we describe briefly the methodology and data employed to estimate $T_e$. For an extensive description of the methods, choice of parameters and biases in $T_e$ estimation, see Supplementary Material associated with the online version of this article.

*2.1. Multitaper method*

To recover spatial variations in $T_e$ we divide the analysis area into overlapping windows, such that in each window the coherence is calculated and inverted assuming a

1   spatially constant $T_e$, moving the centre of each window 50 km for each new estimate.

2   Calculation of the observed and predicted coherence involves transformation into the

3   Fourier domain of the topography and Bouguer gravity anomaly to estimate their auto-

4   and cross-power spectra. Because both data sets are non-periodic and finite, the Fourier

5   transformation presents problems of frequency leakage (Thomson, 1982; Simons et al.,

6   2000), resulting in estimated spectra that differ from the true spectra. To reduce leakage,

7   the data are first multiplied by a set of orthogonal tapers in the space domain, the

8   Fourier transform of the data-taper product taken for each taper, and the power spectrum

9   determined at each taper. The final estimate of the signal's true power spectrum is then

10  the weighted average of the individual power spectra over all tapers. However, the

11  choice of taper influences the resulting power spectra and hence the coherence function

12  (Pérez-Gussinyé et al., 2007, 2008). The set of orthogonal tapers is defined by the

13  bandwidth product $NW$ that controls the wavelength resolution and spectral leakage

14  (where $N$ is the number of samples within the data window and $W$ is the half bandwidth

15  of the central lobe of the power spectral density of the first-order taper) and by the

16  number of tapers $K$ that governs the estimation variance (see Simons et al., 2000). The

17  choice of bandwidth parameter $NW$ in the multitaper technique is important. As the

18  bandwidth increases, the resolution (i.e. the minimum separation in wave number

19  between approximately uncorrelated spectral estimates) decreases (Walden et al., 1995).

20  For a given bandwidth, $W$, there are up to $K = 2NW\text{-}1$ tapers with good leakage

21  properties (Percival and Walden, 1993). The variance of the spectral estimates decreases

22  with the number of tapers as $1/K$, so the bandwidth and resolution are chosen depending

23  on the individual function under analysis (Percival and Walden, 1993). In this study we

24  apply the multitaper method using $NW = 3$ and $K = 3$, which are also used in several

1    recent studies for $T_e$ estimation (see e.g. Daly et al., 2004; Audet et al., 2007; Pérez-

2    Gussinyé et al., 2009a; Kirby and Swain, 2011).

3        The effect of calculating $T_e$ within a finite-size window is to limit the maximum

4    wavelength of the gravity and topography that can be recovered. The choice of window

5    size is critical in the multitaper estimation of $T_e$ because it compromises the trade-off

6    between resolution and variance of the estimates (Pérez-Gussinyé et al., 2004; Audet et

7    al., 2007), such that large windows are better able to retrieve high $T_e$ but degrade the

8    spatial resolution and potentially merge tectonic provinces, while small windows

9    provide high spatial resolution and analyse perhaps just one province but cannot resolve

10   long flexural wavelengths. As the resulting $T_e$ estimate depends on window size, we use

11   three different window sizes (400 x 400 km, 600 x 600 km and 800 x 800 km,

12   respectively) to obtain high spatial resolution and at the same time recover potentially

13   high $T_e$. Finally, the $T_e$ results estimated from three different window sizes are merged

14   to obtain the final $T_e$ map. This is done by calculating a weighted average of the $T_e$

15   estimated from each of the three windows following the approach of Pérez-Gussinyé et

16   al. (2009b). This approach combines the information content regarding abrupt $T_e$

17   gradients recovered by small windows and the more reliable information on high $T_e$

18   recovered by the larger windows.

19

20   *2.2. Wavelet method*

21        The wavelet method convolves a range of scaled wavelets with the whole data

22   set to map and invert the coherence at each grid point, and achieves good wavenumber

23   resolution over long length scales and good spatial resolution over short length scales.

24   Here we employ a Morlet wavelet of high spatial resolution in the fan wavelet transform

1   (Kirby and Swain, 2011). The value of the central wavenumber of the Morlet wavelet,

2   denoted by $|\mathbf{k}_0|$, governs the resolution of the wavelet in the space and wavenumber

3   domains. Larger values of $|\mathbf{k}_0|$ give better wavenumber resolution but poorer spatial

4   resolution, and vice versa for smaller values (Addison, 2002). The choice of the value of

5   $|\mathbf{k}_0|$, described in Kirby and Swain (2011), is governed by the amplitude of the first

6   sidelobes of the simple wavelet. If this amplitude is a fraction $1/p$ ($p > 1$) of the

7   amplitude of the central peak of the real part of the space-domain wavelet, then $|\mathbf{k}_0|$

8   $= \pi\sqrt{2/\ln p}$ . The $|\mathbf{k}_0|$ value used in this study is 2.668, which give a space-domain

9   wavelet whose first sidelobes is 1/16 of the magnitude of the central amplitude (Kirby

10  and Swain, 2011).

11      To recover $T_e$, the Bouguer gravity anomaly and topography are mirrored about

12  their edges prior to Fourier transformation, which, when used with the wavelet

13  transform does not generally bias the results significantly, as it can with the

14  periodogram method (Kirby and Swain, 2008). The wavelet transform is then applied to

15  both datasets to calculate the auto and cross-spectra at different azimuths and scales. We

16  follow Kirby and Swain (2009) and invert the square of the real part of the wavelet

17  coherency (SRC), rather than the coherence, because it is less sensitive to correlations

18  between the initial loads on the plate and to "gravitational noise", both of which can

19  cause incorrect recovery of $T_e$ (Kirby and Swain, 2009, 2011).

20

21  *2.3. Regional topography, gravity and crustal structure*

22      The elevation data used in our analysis are obtained from the ETOPO1 digital

23  elevation model, a 1 arc-minute global relief model of Earth's surface that integrates

24  land topography and ocean bathymetry (Amante and Eakins, 2009). Our area contains

1   both continental and oceanic lithosphere, with the latter being subject to an additional

2   water load. To treat mixed land and marine environments, we adopt the approach of

3   Stark et al. (2003) and Kirby and Swain (2008). This approach scales ocean bathymetry

4   (*h*) to an equivalent topography [ $h' = (\rho_c - \rho_w)h / \rho_c$ ] prior to Fourier transformation,

5   with subsequent application of the land loading deconvolution equations to the entire

6   data set. Kirby and Swain (2008) showed that although this approach may bias $T_e$ in

7   ocean areas, the bias is small. Values of the densities are given in Table 1. The

8   equivalent topography represents the bathymetry that would be expected if there were

9   no water present (provided Airy isostasy operates). This allows the loading equations

10  for a land environment to be used for the whole area, rather than performing two

11  separate analyses and inversions on land and ocean areas (Perez-Gussinye et al., 2004).

12      The regional free-air gravity anomaly data are taken from the V18 Global

13  Gravity Anomaly model of Sandwell and Smith (2009), on a $1' \times 1'$ grid over both land

14  and ocean. The Bouguer gravity anomaly has been calculated applying the complete

15  Bouguer correction at regional scales to free-air data using the FA2BOUG code (Fullea

16  et al., 2008). We calculated terrain corrections using the ETOPO1 digital elevation

17  model (see above), with a reduction density of 2670 kg m$^{-3}$. The Bouguer gravity

18  anomaly of the study area obtained following this procedure is shown in Fig. 2.

19      The deconvolution requires detailed information on the internal structure of the

20  crust and uppermost mantle. To define the internal density profile and lateral variation

21  of the different interfaces, we use the global crustal model CRUST2.0 (Laske and

22  Masters, 1997; Bassin et al., 2000; Laske et al., 2000). CRUST2.0 includes three crustal

23  and two sediment layers, whose 7$^{th}$ layer describes the Moho depth. Forsyth's (1985)

24  original formulation of the predicted coherence assumes that all internal density

1      variations and loading occurs at the Moho. In this study we assumed that internal

2      loading occurs at the interface between upper and mid-crust. Since the observed

3      coherence can be reproduced equally well by either low $T_e$ and shallow loading or a

4      larger $T_e$ and deeper loading, there is a trade-off between $T_e$ and assumed depth of

5      loading. However, Pérez-Gussinyé and Watts (2005) tested the sensitivity of $T_e$ to

6      loading depth in Europe and found that changing the loading depth from the mid-crust

7      to Moho changed $T_e$ by ~5 km, but the general patterns of variations remained the same

8      (Pérez-Gussinyé and Watts, 2005; Pérez-Gussinyé et al., 2007). Other constants are

9      given in Table 1.

10      We project all data sets to a Cartesian coordinate system using the Mercator

11      projection to mitigate errors arising from the planar treatment of curvilinear coordinates.

12      The data cover a much larger area than the study area to mitigate boundary effects.

13

14      **3. Results**

15      *3.1. Spatial variations of $T_e$*

16      The effective elastic thickness obtained from the multitaper and wavelet

17      methods are shown in Fig. 3. Fig. 3a shows the final $T_e$ from multitaper method after

18      merging results from three different window sizes. Fig. 3b shows $T_e$ estimated from the

19      wavelet method with $|\mathbf{k}_0|$=2.668. In the following, we present our results and describe

20      only those $T_e$ variations present in the results obtained with both multitaper and wavelet

21      methods.

22      The pattern of $T_e$ variations in Central America and surrounding regions agrees

23      well with the tectonic provinces in the area, and it is closely related to major tectonic

24      boundaries (Fig. 3). The stable platforms of the North and South American plates have

1  relatively high values. Otherwise, both methods give low values over the southern

2  Cordillera and Baja California areas of North America. A steep $T_e$ gradient separates

3  this region from the southerly regions of the Interior Platform, which are characterized

4  by intermediate to high $T_e$ values (50-100 km). To the east, $T_e$ decreases smoothly

5  towards the Atlantic plain. Over northern South America, we also recover a high $T_e$

6  within the stable platform. Both methods give very large values (> 90 km) over the

7  northern part of the Amazonia craton, where a linear SW-NE trending of much lower $T_e$

8  values characterize the eastern part of the Guyana Shield within the rigid cratonic

9  interior. Northward along the Northern Andes there is an increase of $T_e$ to intermediate

10  values at the junction with the boundary between the South American and Caribbean

11  plates.

12  The northern part of the Maya block shows a linear SW-NE trend of

13  intermediate to high $T_e$ values. The Trans-Mexican Volcanic Belt is characterized by

14  very low $T_e$ values, which are bounded to the south by a narrower band of relatively

15  higher $T_e$. The Maya-Chortis and Chortis-Chorotega active boundaries (i.e., the

16  Polochic-Motagua Fault System and Santa Elena shear zone, respectively) show steep

17  gradients with lower $T_e$ values than the surrounding regions, such that the interaction

18  between these blocks has reduced the strength of the lithosphere near their boundaries.

19  Our results also show a linear NW-SE trending zone of low $T_e$ associated with the

20  Central American volcanic arc, probably associated with high heat flow related to

21  magma transport along the arc (see below). Within the Chortis block, which shows low

22  $T_e$ values, there are two areas of relatively high $T_e$ that coincide with the Nicaraguan

23  depression and the eastern passive margin of this block.

24  Low to intermediate $T_e$ values characterize the Eastern Pacific Ocean, where

1 both methods give extremely low values (<5 km) along region under intensive

2 extension and volcanism, e.g., the East Pacific Rise, around the Galapagos hotspot,

3 Cocos Ridge, Carnegie Ridge and the Cocos-Nazca spreading center, as well as the

4 Cayman spreading center in the Caribbean Sea. The Eastern Pacific also shows

5 contrasting patches of high and low $T_e$. The Middle American subduction zone is

6 characterized by a narrower band of high $T_e$ on the downgoing slab, greater than 30 km,

7 over the outer rise seaward of the trench. These $T_e$ values decrease sharply under the

8 Middle American Trench (MAT) offshore of Central America. In this zone, the

9 Tehuantepec Ridge (TR) represents a major limit which separates the oceanic

10 lithosphere into two distinct tectonic regions with a maximum $T_e$ offset of ~30 km, such

11 that seaward of the trench show higher $T_e$ values in the northwest of the TR than to the

12 southeast of the TR.

13 Over the Gulf of Mexico there is a linear SW-NE trend of intermediate to high

14 $T_e$ values (20-40 km) associated with old oceanic crust (seafloor ages of ~160-120 Myr;

15 Müller et al., 2008) which outcrops in this area. Moreover, most of the Caribbean

16 oceanic domain seems to be uniformly weak. In addition, several patches of

17 intermediate to high $T_e$ are also visible in the Colombian and Venezuelan basins.

18 Westward, the Cocos-Nazca slab window beneath southeastern Costa Rica and

19 northwestern Panamá is characterized by extremely low $T_e$ (< 4 km). Finally, $T_e$

20 increases to high values clearly delineated along the transform plate boundary between

21 the South American and Caribbean plates and Lesser Antilles Trench, which connect

22 northward with the high $T_e$ values in the Puerto Rico Trench, western North Atlantic

23 margin and the Bermuda Rise region.

24 Regardless of the technical differences between the two methods, there is a good

1    overall agreement in the relative spatial variations of $T_e$ recovered from both techniques.

2    Although absolute $T_e$ values can vary in both maps, the qualitative $T_e$ structure and

3    location of the main $T_e$ gradients are very similar. The greater discrepancies between

4    both methods are local spatial variations of $T_e$ in the stable platforms of the North and

5    South American plates. Other differences are observed in $T_e$ values recovered along the

6    plate boundary between the South American and Caribbean plates, northward of the

7    Lesser Antilles Trench and Bermuda Rise region. Since this study focuses on spatial

8    variations of $T_e$ and its geodynamic implications for Central America and surrounding

9    regions, we do not discuss here the differences in absolute values between both maps

10   produced by the methods, and the interested reader can find a more thorough

11   comparison between the wavelet and multitaper methods in, for example, Daly et al.

12   (2004), Audet et al. (2007), Pérez-Gussinyé et al. (2007, 2009a), and Kirby and Swain

13   (2011).

14        As mentioned above, there are several 'key' parameters used in the analysis that

15   lead to small (but perhaps significant) changes in resolution and accuracy of the results

16   from both methods. Here we follow the approach of Pérez-Gussinyé et al. (2009b) and

17   Kirby and Swain (2011) to obtain high spatial resolution and at the same time recover

18   potentially high $T_e$ from both methods. We have included an extensive description of

19   the choice of parameters and its influence on the results, as well as the biases in $T_e$

20   estimation, in the Supplementary Material. It should also be noted that "gravitational

21   noise" (McKenzie and Fairhead, 1997; McKenzie, 2003; Kirby and Swain, 2009) does

22   exist in the study area, which casts doubt upon $T_e$ values in some regions, especially

23   where we have recovered very high values; we will return to this issue in the

24   Discussion.

1

2 *3.2. Comparison with previous $T_e$ estimates*

3       Direct comparison of $T_e$ values and its variations is possible between our results

4 and the previous study of $T_e$ from the multitaper method by Lowry and Pérez-Gussinyé

5 (2011) for the western United States, and with $T_e$ computed by Tassara et al. (2007) and

6 Kirby and Swain (2011) for northern South America using $|\mathbf{k}_0|=2.668$ and $|\mathbf{k}_0|=5.336$

7 wavelets (Supp. Fig. 6 shows our results obtained from wavelet method with

8 $|\mathbf{k}_0|=5.336$). Our results are consistent with these and other previous regional studies of

9 North America (Kirby and Swain, 2009), and South America (Pérez-Gussinyé et al.,

10 2007, 2008, 2009a). This consistency indicates the viability of our results over Central

11 America and surrounding regions.

12       Regarding the Central America region, there are numerous studies of oceanic $T_e$

13 performed for given places (for a compilation see Watts, 2001). For the Middle America

14 Trench, Caldwell and Turcotte (1979) estimated a $T_e$ of 18.6±2.2 km for seafloor age of

15 32.5±2.5 Myr. Meanwhile, McNutt (1984) obtained a $T_e$ of 17.5±2.5 km for 20±5 Myr,

16 McAdoo and Martin (1984) a $T_e$ of 29.7±2.2 km for 20±5 Myr, and Levitt and Sandwell

17 (1995) a $T_e$ of 27.3±10 km for 19.9±8 Myr. Feighner and Richards (1994) studied the

18 Galápagos region using a variety of compensation models, obtaining a $T_e$ of 12±2 km

19 and 3±3 km for 7.5±1 Myr. McAdoo et al. (1985) obtained a $T_e$ of 31.7±5.2 km for

20 80±5 Myr over the Puerto Rico Trench, and Levitt and Sandwell (1995) a $T_e$ of 40.7±5

21 km for 101.6±12 Myr over the Antilles Trench. Furthermore, in their study Manea et al.

22 (2005) estimated $T_e$ of the oceanic lithosphere beneath Tehuantepec Ridge by means of

23 an admittance analysis of a set of profiles across this structure. These authors obtained a

24 $T_e$ of ~5-10 km in the NW area of the TR, while in the SE area $T_e$ is of ~10-15 km. As

1  mentioned above, we recover a complex pattern of $T_e$ associated with the TR, with a

2  maximum offset of ~30 km.

3  Finally, our results are in a good agreement with previous global studies as in

4  e.g., Watts et al. (2006), who obtained $T_e$ estimates from a wide range of submarine

5  volcanic features in the East Pacific Ocean. Recently, Kalnins (2011) produced a global

6  map of elastic thickness in the world's oceans, and recovered $T_e$ at major constructional

7  volcanic features in our study area, as the Bermuda Rise ($T_e$ of 15-21 km), Carnegie

8  Ridge (3-4 km), Cocos Ridge (3-4 km), Galapagos Islands (3-4 km) or Nazca Ridge (4-

9  5 km). Furthermore, our results are also in a good agreement with the worldwide $T_e$ map

10  obtained by Audet and Bürgmann (2011) from the Bouguer coherence using the

11  continuous wavelet transform, and with $T_e$ results of Tesauro et al. (2012) from a

12  rheological approach based on the lithospheric strength distribution, although our results

13  have higher resolution due to the regional nature of the present work.

14

15  **4. Discussion**

16  *4.1. $T_e$, surface heat flow and thermal age*

17  Due to the dependence of lithosphere strength on temperature, $T_e$ should show

18  an inverse correlation with heat flow (McNutt, 1984; Lowry and Smith, 1995): higher

19  surface heat flow implies higher lithospheric temperatures and hence lower lithospheric

20  strength. Several studies examining the dependence of the strength of the lithosphere on

21  the temperature structure (e.g., Watts and Burov, 2003; Afonso and Ranalli, 2004;

22  Burov and Watts, 2006), found that there is not a simple relation between $T_e$ and surface

23  heat flow for continental areas, due to local differences in crustal structure and

24  composition (which implies differences in radioactive heat production and thermal and

1    rheological properties of the rocks) and lithosphere flexure (which affects the vertical

2    distribution of elastic stresses). Otherwise, the situation is relatively simpler for oceanic

3    areas, because oceanic crust is thinner and comparatively devoid of radioactive

4    elements, implying that the strength of the lithosphere is mostly controlled by the

5    cooling history (i.e., thermal age) of the oceanic lithosphere, although flexural effects

6    can be important.

7         Fig. 4a shows the regional surface heat flow in the study area from the updated

8    global heat flow database of the International Heat Flow Commission (Hasterok, 2010).

9    Despite some uncertainties, there is a relatively good (inverse) correlation between

10   surface heat flow and $T_e$ values in Central America and surrounding regions. Low $T_e$

11   values observed in the southern Cordillera and Baja California are associated with

12   relatively high heat flow. Similarly, high $T_e$ values recovered for southern regions of the

13   Interior Platform match the observed low heat flow (Fig. 3 and Fig. 4a). By contrast,

14   there are extensive areas with no measurements, e.g., the northern South America.

15   Pérez-Gussinyé et al. (2007, 2008) examined the relationship of $T_e$ to heat flow in South

16   America, concluding that both parameters correlate well. Our relatively high $T_e$ values

17   observed in the northern part of the Maya block and in the southern boundary of the

18   Trans-Mexican Volcanic Belt are well correlated with the low surface heat flow of these

19   areas. The Trans-Mexican Volcanic Belt is characterized by intermediate to high heat

20   flow and low $T_e$ values. The southern Maya block and northwestern Chortis block,

21   including the northwestern Central American volcanic arc, are also characterized by

22   high surface heat flow and low $T_e$ values. By contrast, the southeastern part of the

23   Central American volcanic arc and Chorotega block are characterized by low heat flow

24   and low $T_e$ values (Fig. 3 and Fig. 4a), such that it's possible that due to the narrow

1    width of the Central American land bridge in this area, the $T_e$ recovered over the

2    continent is very influenced by the low $T_e$ values of the surrounding oceanic regions.

3    As illustrated in Fig. 4a, high heat flow is observed in the Eastern Pacific Ocean

4    in regions under intensive extension and volcanism, e.g. the East Pacific Rise, around

5    the Galapagos hotspot, Cocos Ridge, Carnegie Ridge and the Cocos-Nazca spreading

6    center, as well as over the Cayman spreading center in the Caribbean Sea. This first-

7    order pattern of surface heat flow variation is in accord with our low $T_e$ estimates for

8    these areas (Fig. 3). However, a low heat flow is observed within the Cocos plate where

9    there is not a clear correlation with the $T_e$ signature associated to the Middle American

10   subduction zone (see below). The western Caribbean region shows moderate surface

11   heat flow, where the Cocos-Nazca slab window beneath Central America, characterized

12   by extremely low $T_e$, does not show a high surface heat flow. Meanwhile the eastern

13   Caribbean region is characterized by lower values, with several contrasting patches of

14   high surface heat flow as in the central part of the Hess Escarpment or over the Aves

15   Ridge associated with the Lesser Antilles.

16   It is commonly accepted that $T_e$ reflects a fossil lithospheric equilibrium

17   developed at the time of loading (for a review see Artemieva, 2011). If loading occurs

18   when the lithosphere is weak and no mass redistribution occurs afterwards, there is no

19   need for stress to re-equilibrate, and isostatic analyses might yield a low $T_e$ estimate

20   even after subsequent cooling and strengthening of the lithosphere, as is the case for

21   oceanic lithosphere (Pérez-Gussinyé et al., 2009b). Fig. 4b shows the age-area

22   distribution of the ocean floor from Müller et al. (2008) in the study area. If we compare

23   our $T_e$ results with the age of the ocean crust in the study area (Fig. 4c), a direct

24   relationship between them is not evident. This is consistent with the scatter observed in

1     previous works on other oceanic regions (e.g., Tassara et al., 2007; Kalnins and Watts,

2     2009). Watts (2001) notes that the load age, which is not necessarily the same of the

3     crust age, would explain much of this scatter. Other contributing sources could be

4     uncertainties in load, infill and mantle densities, thermal perturbations due to hot and

5     cold spots (e.g., Tassara et al., 2007), viscoelastic stress relaxation (Watts and Zhong,

6     2000), yielding in regions of large loads and high curvature (McNutt and Menard,

7     1982), or spatial variations in the controlling isotherms that determine $T_e$ (Kalnins and

8     Watts, 2009).

9         Otherwise, as stated above, the thermal state and rheological behaviour of the

10    lithosphere in continental areas are largely a consequence of local conditions, such that

11    there is a complex relationship between $T_e$ and the age of the continental lithosphere.

12    Surface processes of erosion and deposition constantly redistribute continental surface

13    mass loads. In any case, the high $T_e$ values recovered here for the stable platforms of the

14    North and South American plates (see Fig. 3) are consistent with previous studies for

15    these regions (Tassara et al., 2007; Pérez-Gussinyé et al., 2007, 2009a; Kirby and

16    Swain, 2009, 2011).

17

18    *4.2. Loading of the lithosphere*

19         A fundamental assumption of the load deconvolution method developed by

20    Forsyth (1985) is that surface and subsurface loads are statistically uncorrelated. In

21    many cases, however, surface and subsurface loading are likely to be tectonically

22    related processes and, therefore, spatially correlated (Forsyth, 1985). Subsurface loads

23    include mafic intrusions, accreted lower crustal material, thermal anomalies and

24    compositional variations, which cause lateral variations of density at depth and may

1    have a strong influence on $T_e$ estimates (Stark et al., 2003). Meanwhile, surface loading

2    is caused by topography and large-scale variations in surface density (e.g., mountains

3    and sedimentary basin). Macario et al. (1995) showed that when the degree of

4    correlation of initial surface and subsurface loading increases, the $T_e$ values estimated

5    using Forsyth's (1985) deconvolution method can be biased downward. Furthermore,

6    erosion and sedimentation may play an important role in modifying the relationship

7    between surface topography and subsurface density anomalies (e.g., Forsyth, 1985;

8    McKenzie and Fairhead, 1997). Both processes can reduce the landscape to a perfectly

9    flat surface, removing the topographic expression of subsurface loads. The presence of

10   topographically unexpressed internal loading, known as "noise" or "gravitational noise"

11   (McKenzie and Fairhead, 1997; McKenzie, 2003; Kirby and Swain, 2009), biases the $T_e$

12   upward. As pointed out by Kirby and Swain (2009), this problem can occur in regions

13   of subdued topography, and predominantly affects areas where the coherence method

14   indicates high $T_e$ (see Suppl. Fig. 7).

15   The load deconvolution wavelet method can also estimate the ratio between the

16   initial internal and surface load amplitudes (the loading ratio, $f$; Forsyth, 1985). We can

17   display the loading ratio results in terms of the $F$ parameter, the internal load fraction

18   (McKenzie, 2003), where purely surface loading gives $F = 0$, purely internal loading

19   gives $F = 1$, while equal surface and internal loading gives $F = 0.5$ (see Supplementary

20   Material for an extended explanation). Fig. 5a shows best fitting $F$ values corresponding

21   to the $T_e$ recovered from the wavelet method (Fig. 3b). For North America, our results

22   are consistent with Kirby and Swain's (2009) $F$ results, which show that subsurface

23   loading has dominated continental tectonics, or at least been equal in magnitude to

24   surface loading, in North America. Our results are also consistent with the pattern of the

1    flexural loading ratio, $f_F$, obtained by Tassara et al. (2007) in northern South America,

2    which suggest that below the north-eastern limit of the Amazonia craton there are strong

3    lateral variations in density not compensated by surface topography. Subsurface loading

4    dominates along the East Pacific Rise, around the Galapagos hotspot, Cocos Ridge,

5    Carnegie Ridge and the Cocos-Nazca spreading center (Fig. 5a). In this zone, the

6    Tehuantepec Ridge represents, again, a major limit which separates the oceanic

7    lithosphere into two distinct load regions, such that the northwest TR is dominated by

8    surface loading while the southeast TR is dominated by internal loads. The Caribbean

9    region is characterized by all range of $F$ values. Higher $F$ values are observed over the

10    eastern Cayman spreading center, the Caribbean Large Igneous Province, the Cocos-

11    Nazca slab window beneath Central America, the Aves Ridge, and along the Lesser

12    Antilles Trench and east North American margin.

13        Fig. 5b shows seafloor sediment thickness (Divins, 2003; Whittaker et al., 2013)

14    in the study area. Large amount of sediments are located on the Gulf of Mexico basin,

15    along of the western North Atlantic margin, the Colombian, Venezuelan and Grenada

16    basins, and on the Barbados Accretionary Complex associated to the Lesser Antilles. In

17    many cases sediment thickness exceeds 10 km. However, most of the Caribbean

18    lithosphere, where both methods recovered low $T_e$ values (see Fig. 3), seems to be

19    uniformly weak, suggesting that the effect of the sediments on $T_e$ estimates is very

20    small. The continental shelf of the Gulf of Mexico, which shows a smooth surface, is

21    characterized by moderate to high $T_e$ values (between 40-50 km; see Fig. 3) and low $F$

22    values, with surface loads dominating. Seaward, high $T_e$ values are recovered for the

23    Mississippi delta system (Fig. 3). Southwestward in the Gulf of Mexico, over the old

24    oceanic crust which outcrops in this area, both methods recover a linear SW-NE

1  trending of intermediate to high $T_e$ values associated with a high $F$ value. The

2  Venezuelan basin also shows high $T_e$ values associated with a subsurface loading

3  domain, possibly related to the oceanic basement underneath the Caribbean Large

4  Igneous Province. Müller et al. (2008) found prominent negative residual basement

5  depth anomalies (in a range between 750 and 1500 m) associated with the Gulf of

6  Mexico, northeast of Venezuela, and off the east coast of North America, which may be

7  related to subducted slab material descending in the mantle or to asthenospheric flow.

8  In the case of the Colombian basin, the presence of sediments on the continental shelf

9  may play a major role on the estimation of $T_e$ (~40 km; Fig. 3 and Fig. 5b).

10  Interestingly, the presently active Nicaraguan depression, which experienced significant

11  extension in the Cenozoic, shows intermediate $T_e$ values (~25 km) and a $F$ value of 0.5,

12  such that it is possible that in this case $T_e$ values are overestimated due to the effect

13  associated with its sediment fill (see Suppl. Fig. 7).

14

15  *4.3. The Middle American and Lesser Antilles subduction zones*

16  The results over the Middle American and Lesser Antilles subduction zones

17  should be interpreted with caution. As exposed in the Results Section, the Middle

18  American subduction zone is characterized by a narrower band of high $T_e$ on the

19  downgoing slab seaward of the trench (Fig. 3). These $T_e$ values decrease sharply under

20  the MAT offshore of Central America, indicating a substantial degree of weakening

21  within the downgoing plate due to the flexure of the lithosphere (see McNutt and

22  Menard, 1982; Judge and McNutt, 1991; Billen and Gurnis, 2005; Contreras-Reyes and

23  Osses, 2010). In fact, the bathymetry of the MAT offshore of Central America shows a

24  complex response of the crust to the subduction process, with widespread outer-rise

1  normal faulting subparallel to the trench axis due to the plate bending, increasing in

2  number and offset where the bending is more pronounced (Ranero et al., 2003, 2005;

3  Harders et al. 2011; Manea et al., 2013). This high $T_e$ signature is very evident (broader

4  and even exceeding 50 km at the Lesser Antilles Trench; see Fig. 3), and can also be

5  observed in other subduction zones, as e.g. along the Peru-Chile Trench (Tassara et al.,

6  2007; Pérez-Gussinyé et al., 2009a; Kirby and Swain, 2011), or over the Japan, Izu-

7  Bonin, and Mariana trenches and at the northernmost tip of the Tonga-Kermadec trench

8  (Kalnins and Watts, 2009).

9        Subsurface loads, such as those due to a dense downgoing slab, should be taken

10  into account when interpreting the results over subduction zones (Kalnins and Watts,

11  2009). We have found that the high $T_e$ values over the Middle American and Lesser

12  Antilles subduction zones are dominated by internal loads (and in the case of the

13  southernmost tip of the LAT also associated with a large amount of sediments; see Fig.

14  5), where the corresponding noise levels are high (see Suppl. Fig. 7) and thus, these

15  results may be biased upward. If $T_e$ over the Middle American subduction zone is

16  actually low (at least relatively), it would be in accordance with they reflecting a

17  "frozen in" signal which is not affected in this zone by subsequent cooling and

18  strengthening of the oceanic lithosphere. Interestingly, this is not the case of the Lesser

19  Antilles subduction zone, where the high $T_e$ values are free of noise (excepting the

20  southernmost tip of the LAT associated with a large amount of sediments; see Fig.5b

21  and Suppl. Fig. 7), and persist in all our results from different window sizes and $|\mathbf{k}_0|$ in

22  both multitaper and wavelet methods, respectively (see Fig.3 and Supp. Fig. 1 and 6).

23  This is in accordance with the strength of the oceanic lithosphere is being in this case

24  controlled by the thermal age of the lithosphere at the time of loading (Watts, 2001;

1 Kalnins and Watts, 2009), such that $T_e$ values increase with cooling of the oceanic

2 lithosphere away from the ridge. Furthermore, it should be noted that the results over

3 the Middle American and Lesser Antilles subduction zones, especially in relation to the

4 high gradient that limits these bands of higher $T_e$, are highly dependent on the choice of

5 spectral parameters in both multitaper and wavelet methods (see Fig.3 and Supp. Fig. 1

6 and 6).

7

8 *4.4. $T_e$ and seismicity*

9 The magnitude and spatial variations of $T_e$ could control the degree, style and

10 localization of deformation in response to long-term tectonic loads, and potentially the

11 distribution of seismic activity (e.g., Lowry and smith, 1995; Tassara et al., 2007; Audet

12 and Bürgmann, 2011; Chen et al., 2013). The seismotectonics of the circum-Caribbean

13 area is complex, and essentially related to plate boundaries, with intraplate activity

14 being very scarce (Fig. 6a). Comparison of the spatial variation of $T_e$ with the shallow

15 (< 50 km deep) earthquake distribution indicates that most of the seismic activity is

16 located in regions with low $T_e$ or steep $T_e$ gradient, while the lack of seismicity in stable

17 tectonic provinces characterized by high $T_e$ values is evident (Fig. 6a). As illustrated in

18 Fig. 6b, shallow earthquakes are very frequent in regions with low $T_e$ (< 20 km), and are

19 relatively scarce in regions with higher values. This suggests that the stronger

20 lithosphere resists deformation and transfers the stress effectively, while the weak

21 lithosphere and areas with steep change of $T_e$ are prone to accumulate and then release

22 tectonic stresses causing earthquakes (Mao et al., 2012; Chen et al., 2013).

23

24

1    **5. Conclusions**

2    We have used two different spectral methods (multitaper and wavelet) to

3    calculate the coherence between the Bouguer gravity anomaly and the topography in

4    order to estimate the spatial variations in effective elastic thickness in Central America

5    and surrounding regions. We have generated, for the first time, high-resolution maps of

6    spatial variations of $T_e$ for this region. Regardless of the technical differences between

7    the two methods, there is a good overall agreement in the spatial variations of $T_e$

8    recovered from both methods. Although absolute $T_e$ values can vary in both maps, the

9    qualitative $T_e$ structure and location of the main $T_e$ gradients are very similar, such that

10   estimation of $T_e$ is relatively insensitive to the choice of spectral estimator.

11   The pattern of the $T_e$ variations in Central America and surrounding regions

12   agrees well with the tectonic provinces in the region, and it is closely related to major

13   tectonic boundaries. There is a relatively good correlation, despite some uncertainties,

14   between surface heat flow and our $T_e$ results. These results suggest that although this

15   area is geologically complex, the thermal state of the lithosphere has profound influence

16   on its strength, such that $T_e$ is strongly governed by thermal structure. Otherwise, in

17   general there is not a direct relationship between $T_e$ and the age of the ocean crust in of

18   our study area (contrary to that expected if $T_e$ is exclusively controlled by the thermal

19   structure of the oceanic lithosphere), which could be explained for other factors, maybe

20   mainly differences in age loading.

21   The Middle American and Lesser Antilles subduction zones are characterized by

22   a band of high $T_e$ on the downgoing slab seaward of the trenches. These high $T_e$ values

23   are related to internal loads (and in the case of the southernmost tip of the LAT also

24   associated with a large amount of sediments); showing high noise levels and they may

be biased upward. Thus, the results over subduction zones should be interpreted with caution, and warrant further analysis.

Finally, future research should also evaluate the relationship between $T_e$, as well as its anisotropy, Moho structure and mantle structure within a geodynamical perspective, in order to improve our understanding on the evolution of the Caribbean plate.

**Appendix A. Supporting information**

Supplementary material associated with this article can be found in the online version at http://

1   **References**

2   Addison, P.S., 2002. The Illustrated Wavelet Transform Handbook, Institute of Physics

3        Publishing, Bristol, UK.

4   Afonso, J.C., Ranalli, G., 2004. Crustal and mantle strengths in continental lithosphere:

5        is the jelly sandwich model obsolete? Tectonophysics, 394, 221-232.

6   Amante, C., Eakins, B.W., 2009. ETOPO1 1 Arc-Minute Global Relief Model:

7        Procedures, Data Sources and Analysis. NOAA Technical Memorandum NESDIS

8        NGDC-24, 19 pp, March 2009.

9   Artemieva, I., 2011. The Lithosphere: An Interdisciplinary Approach. Cambridge

10        University Press (773 pp.).

11   Audet, P., Bürgmann, R., 2011. Dominant role of tectonic inheritance in supercontinent

12        cycles. Nature Geoscience 4, 184-187.

13   Audet, P., Jellinek, A.M., Uno, H., 2007. Mechanical controls on the deformation of

14        continents at convergent margins. Earth and Planetary Science Letters 264, 151-

15        166.

16   Bassin, C., Laske, G., Masters, T.G., 2000. The current limits of resolution for surface

17        wave tomography in North America. Eos, Transactions American Geophysical

18        Union 81, F897.

19   Billen, M.I. and Gurnis, M., 2005. Constraints on subducting plate strength within the

20        Kermadec trench. J. Gophys. Res., 110, B05407.

21   Bird, P., 2003. An updated digital model of plate boundaries. Geochemistry Geophysics

22        Geosystems, 4(3), 1027, doi:10.1029/2001GC000252.

23   Bürgmann, R., Dresen, G., 2008. Rheology of the lower crust and upper mantle:

24        evidence from rock mechanics, geodesy, and filed observations. Annual Review

1      of Earth and Planetary Sciences 36, 531-567.

2    Burov, E.B, 2011. Rheology and strength of the lithosphere. Marine and Petroleum

3      Geology 28, 1402-1443.

4    Burov, E.B., Diament, M., 1995. The effective elastic thickness of (Te) continental

5      lithosphere. What does it really means? J. Geophys. Res. 100 (B3), 3905-3927.

6    Burov, E.B., Watts, A.B., 2006. The long-term strength of continental lithosphere:

7      "jelly sandwich" or "crème brûlée"? GSA Today 16 (1), 4-10.

8    Caldwell, J.G. and Turcotte, D.L., 1979. Dependence of the elastic thickness of the

9      oceanic lithosphere on age. J. Geophys. Res. 84, 7572-7576.

10   Chen, B., Chen, C., Kaban, M.K., Du, J., Liang, Q., Thomas, M., 2013. Variations of

11     the effective elastic thickness over China and surroundings and their relation to

12     the lithosphere dynamics. Earth and Planetary Science Letters 363, 61-72.

13   Contreras-Reyes, E., Osses, A., 2010. Lithospheric flexure modeling seaward of the

14     Chile trench: implications for oceanic plate weakening in the Trench Outer Rise

15     region. Geophysical Journal International 182 (1), 97-112.

16   Daly, E., Brown, C., Stark, C.P., Ebinger, C.J., 2004. Wavelet and multitaper coherence

17     methods for assessing the elastic thickness of the Irish Atlantic margin. Geophys.

18     J. Int., 159, 445-459.

19   DeMets, C., Gordon, R.G., Argus, D.F., 2010. Geologically current plate motions.

20     Geophys. J. Int., 181, 1-80, doi: 10.1111/j.1365-246X.2009.04491.x, 2010. see

21     also Erratum, Geophys. J. Int., 0, 1-1, doi: 10.1111/j.1365-246X.2011.05186.x,

22     2011.

23   Divins, D.L., 2003. Total Sediment Thickness of the World's Oceans & Marginal Seas,

24     NOAA National Geophysical Data Center, Boulder, CO.

1  Ekström, G., Nettles, M., Dziewoński, A., 2012. The global CMT project 2004-2010:

2      centroid-moment tensors for 13,017 earthquakes. Physics of the Earth and

3      Planetary Interiors 200-201, 1-9.

4  Feighner, M.A., Richards, M.A., 1994. Lithospheric structure and compensation

5      mechanism of the Galápagos Arc. J. Geophys. Res. 99, 6711-6729.

6  Forsyth, D.W., 1985. Subsurface loading estimates of the flexural rigidity of continental

7      lithosphere. J. Geophys. Res. 90, 12,623-12,632.

8  Fullea, J., Fernàndez, M., Zeyen, H., 2008. FA2BOUG - A FORTRAN 90 code to

9      compute Bouguer gravity anomalies from gridded free air anomalies: application

10     to the Atlantic–Mediterranean transition zone. Computers & Geosciences 34,

11     1665-1681.

12 Harders, R., Ranero, C.R., Weinrebe, W., Behrmann, J.H., 2011. Submarine slope

13     failures along the convergent continental margin of the Middle America Trench.

14     Geochem. Geophys. Geosyst., 12, Q05S32.

15 Hasterok, D., 2010. Thermal state of the Oceanic and Continental Lithosphere. Ph.D.

16     Thesis, University of Utah.

17 Hasterok, D., Chapman, D.S., 2011. Heat production and geotherms for the continental

18     lithosphere. Earth and Planetary Science Letters 307, 59-70.

19 Judge, A.V., McNutt, M.K., 1991. The Relationship Between Plate Curvature and

20     Elastic Plate Thickness: A Study of the Peru-Chile Trench, J. geophys. Res.,

21     96(B10), 16 625-16 639.

22 Kalnins, L.M., 2011. Spatial Variations in the Effective Elastic Thickness of the

23     Lithosphere and their Tectonic Implications. Ph.D. Thesis. University of Oxford.

24 Kalnins, L.M., Watts, A.B., 2009. Spatial variations in effective elastic thickness in the

1    Western Pacific Ocean and their implications for Mesozoic volcanism. Earth and

2    Planetary Science Letters 286, 89-100.

3    Kirby, J.F., Swain, C.J., 2008. An accuracy assessment of the fanwavelet coherence

4    method for elastic thickness estimation. Geochemistry, Geophysics, Geosystems 9

5    (3), Q03022. (Correction. 2008. Geochemistry, Geophysics, Geosystems 9(5),

6    Q05021).

7    Kirby, J.F., Swain, C.J., 2009. A reassessment of spectral Te estimation in continental

8    interiors: the case of North America. Journal of Geophysical Research 114,

9    B08401.

10   Kirby, J.F., Swain, C.J., 2011. Improving the spatial resolution of effective elastic

11   thickness estimation with the fan wavelet transform. Computers & Geosciences

12   37, 1345-1354.

13   Laske, G., Masters, G., 1997. A global digital map of sediment thickness. Eos,

14   Transactions American Geophysical Union 78, F483.

15   Laske, G., Masters, G., Reif, C., 2000. A New Global Crustal Model at 2×2 Degrees

16   (CRUST2.0). http://igppweb.ucsd.edu/~gabi/rem.dir/crust/crust2.html.

17   Levitt, D.A., Sandwell, D.T., 1995. Lithospheric bending at subduction zones based on

18   depth soundings and satellite gravity, J. Geophys. Res., 100, 379-400.

19   Lowry, A.R., Pérez-Gussinyé, M., 2011. The role of crustal quartz in controlling

20   Cordilleran deformation. Nature 471(7338), 353-357. doi:10.1038/nature09912

21   Lowry, A.R., Ribe, N.M., Smith, R.B., 2000. Dynamic elevation of the Cordillera,

22   western United States. J. Geophys. Res. 105, 23,371-23,390.

23   Lowry, A.R., Smith, R.B., 1995. Strength and rheology of the western U.S. Cordillera.

24   J. Geophys. Res. 100, 17,947-17,963.

1     Macario, A., Malinverno, A., Haxby, W.F., 1995. Onthe robustness of elastic thickness

2         estimates obtained using the coherence method. J. Geophys. Res. 100 (D8),

3         15,163-15,172.

4     Manea, M., Manea, V.C., Kostoglodov, V., Guzman-Speziale, M., 2005. Elastic

5         thickness of the lithosphere below the Tehuantepec Ridge. Geofis. Int. 44, 2157-

6         168.

7     Manea, V.C., Manea, M., Ferrari, L., 2013. A geodynamical perspective on the

8         subduction of Cocos and Rivera plates beneath Mexico and Central America.

9         Tectonophysics 609, 56-81.

10    Mao, X., Wang, Q., Liu, S., Xu, M., Wang, L., 2012. Effective elastic thickness and

11        mechanical anisotropy of South China and surrounding regions. Tectonophysics

12        550-553, 47–56.

13    Mareschal, J-C., Jaupart, C., 2013. Radiogenic Heat Production, Thermal Regime and

14        Evolution of Continental Crust. Tectonophysics 609, 524-534.

15    McAdoo, D.C., Martin, C.F., 1984. Seasat observation of geoid anomalies due to

16        subducting slabs. J. Geophys. Res. 87, 8684-8692.

17    McAdoo, D.C., Martin, C.F., Poulose, S., 1985. Seasat observations of flexure:

18        Evidence for a strong lithosphere. Tectonophysics, 116, 209-222.

19    McKenzie, D., 2003. Estimating Te in the presence of internal loads. Journal of

20        Geophysical Research 108 (B9), 2438.

21    McKenzie, D.P., Fairhead, J.D., 1997. Estimates of the effective elastic thickness of the

22        continental lithosphere from Bouguer and free air gravity anomalies. J. geophys.

23        Res., 102(B12), 27 523-27 552.

24    McNutt, M.K., 1984. Lithospheric flexure and thermal anomalies, J. Geophys. Res., 89,

1    11 180-11 194.

2    McNutt, M.K., Menard, H.W., 1982. Constraints on yield strength in the oceanic

3        lithosphere derived from observations of flexure. Geophys. J. R. Astr. Soc., 71,

4        363-394.

5    Müller, R.D., Sdrolias, M., Gaina, C., Roest, W.R., 2008. Age, spreading rates, and

6        spreading asymmetry of the world's ocean crust. Geochem. Geophys. Geosyst., 9,

7        Q04006.

8    Percival, D.B., Walden, A.T., 1993. Spectral Analysis for Physical Applications,

9        Multitaper and Conventional Univariate Techniques, pp. 1-190, Cambridge Univ.

10       Press, New York.

11   Pérez-Gussinyé, M., Lowry, A.R., Watts, A.B., Velicogna, I., 2004. On the recovery of

12       the effective elastic thickness using spectral methods: examples from synthetic

13       data and from the Fennoscandian Shield. J. Geophys. Res. 109.

14   Pérez-Gussinyé, M., Watts, A.B., 2005. The long-term strength of Europe and its

15       implications for plate forming processes. Nature 436, 381-384.

16   Pérez-Gussinyé, M., Lowry, A.R., Watts, A.B., 2007. Effective elastic thickness of

17       South America and its implications for intracontinental deformation. Geochem.

18       Geophys. Geosyst. 8 (5), Q05009.

19   Pérez-Gussinyé, M., Lowry, A.R., Phipps Morgan, J., Tassara, A., 2008. Effective

20       elastic thickness variations along the Andean margin and their relationship to

21       subduction geometry. Geochem. Geophys. Geosyst. 9, Q02003.

22   Pérez-Gussinyé, M., Swain, C.J., Kirby, J.F., Lowry, A.R., 2009a. Spatial variations of

23       the effective elastic thickness, Te, using multitaper spectral estimation and

24       wavelet methods: examples from synthetic data and application to South America.

Geochem. Geophys. Geosyst. 10, Q04005.

Pérez-Gussinyé, M., Metois, M., Fernández, M., Vergés, J., Fullea, J., Lowry, A.R., 2009b. Effective elastic thickness of Africa and its relationship to other proxies for lithospheric structure and surface tectonics. Earth and Planetary Science Letters 287, 152-167.

Ranalli, G., 1997. Rheology of the lithosphere in space and time. Geol. Soc. Spec. Pub. 121, 19-37.

Ranero, C.R., Morgan, J.P., McIntosh, K., Reichert, C., 2003. Bending-related faulting and mantle serpentinization at the Middle America trench. Nature 425, 367-373.

Ranero, C.R., Villaseñor, A., Morgan, J.P., Weinrebe, W., 2005. Relationship between bend-faulting at trenches and intermediate-depth seismicity. Geochem. Geophys. Geosyst., 6, Q12002.

Ross, M.I., Scotese, C.R., 1988, A hierarchical tectonic model of the Gulf of Mexico and Caribbean region, Tectonophysics 155, 139-168.

Sandwell, D.T., Smith, W.H.F., 2009. Global marine gravity from retracked Geosat and ERS-1 altimetry: ridge segmentation versus spreading rate. Journal of Geophysical Research 114, B01411.

Siebert, L., Simkin, T., 2002. Volcanoes of the world: an illustrated catalog of Holocene volcanoes and their eruptions. Smithsonian Institution, Global Volcanism Program Digital Information Series, GVP-3. http://www.volcano.si.edu/world/.

Simons, F.J., Zuber, M.T., Korenaga, J., 2000. Isostatic response of the Australian lithosphere: estimation of effective elastic thickness and anisotropy using multitaper spectral analysis. Journal of Geophysical Research 105 (B8), 19,163-19,184.

1 Stark, C.P., Stewart, J., Ebinger, C.J., 2003. Wavelet transform mapping of effective
2    elastic thickness and plate loading: validation using synthetic data and application
3    to the study of southern African tectonics. J. Geophys. Res. 108 (B12), 2558.

4 Sykes, L.R., McCann, W.R., Kafka, A.L. 1982. Motion of Caribbean Plate during last 7
5    million years and implications for early Cenozoic movements. J. Geophys. Res.
6    87, B13, 10656-10676.

7 Tassara, A., Swain, C.J., Hackney, R.I., Kirby, J.F., 2007. Elastic thickness structure of
8    South America estimated using wavelets and satellite-derived gravity data. Earth
9    and Planetary Science Letters 253, 17-36.

10 Tesauro, M., Kaban, M.K., Cloetingh, S.A.P.L., 2012. Global strength and elastic
11    thickness of the lithosphere. Global and Planetary Change 90-91, 51-57.

12 Thomson, D.J., 1982. Spectrum estimation and harmonic-analysis. Proceedings of the
13    IEEE 70 (9), 1055-1096.

14 Walden, A. T., McCoy, E. J., Percival, D. B., 1995. The effective bandwidth of a
15    multitaper spectral estimator. Biometrika, 82(1), 201-214.

16 Watts, A.B., 2001. Isostasy and Flexure of the Lithosphere. Cambridge University
17    Press. 472 pp.

18 Watts, A.B., Burov, E.B, 2003. Lithospheric strength and its relation to the elastic and
19    seismogenetic layer thickness. Earth and Planetary Science Letters 213, 113-131.

20 Watts, A.B., Sandwell, D.T., Smith, W.H.F., Wessel, P., 2006. Global gravity,
21    bathymetry, and the distribution of submarine volcanism through space and time.
22    J. Geophys. Res. 111 (B8).

23 Watts, A.B., Zhong, S., 2000. Observations of flexure and the rheology of oceanic
24    lithosphere. Geophys. J. Int. 142 (3), 855-875.

1   Wessel, P., Smith, W.H.F., Scharroo, R., Luis, J.F., Wobbe, F., 2013. Generic Mapping

2       Tools: Improved version released, EOS Trans. AGU, 94, 409-410.

3   Whittaker, J., Goncharov, A., Williams, S., Müller, R.D., Leitchenkov, G., 2013. Global

4       sediment thickness dataset updated for the Australian-Antarctic Southern Ocean.

5       Geochem. Geophys. Geosyst. 14 (8), 2547-3313. DOI: 10.1002/ggge.20181

6
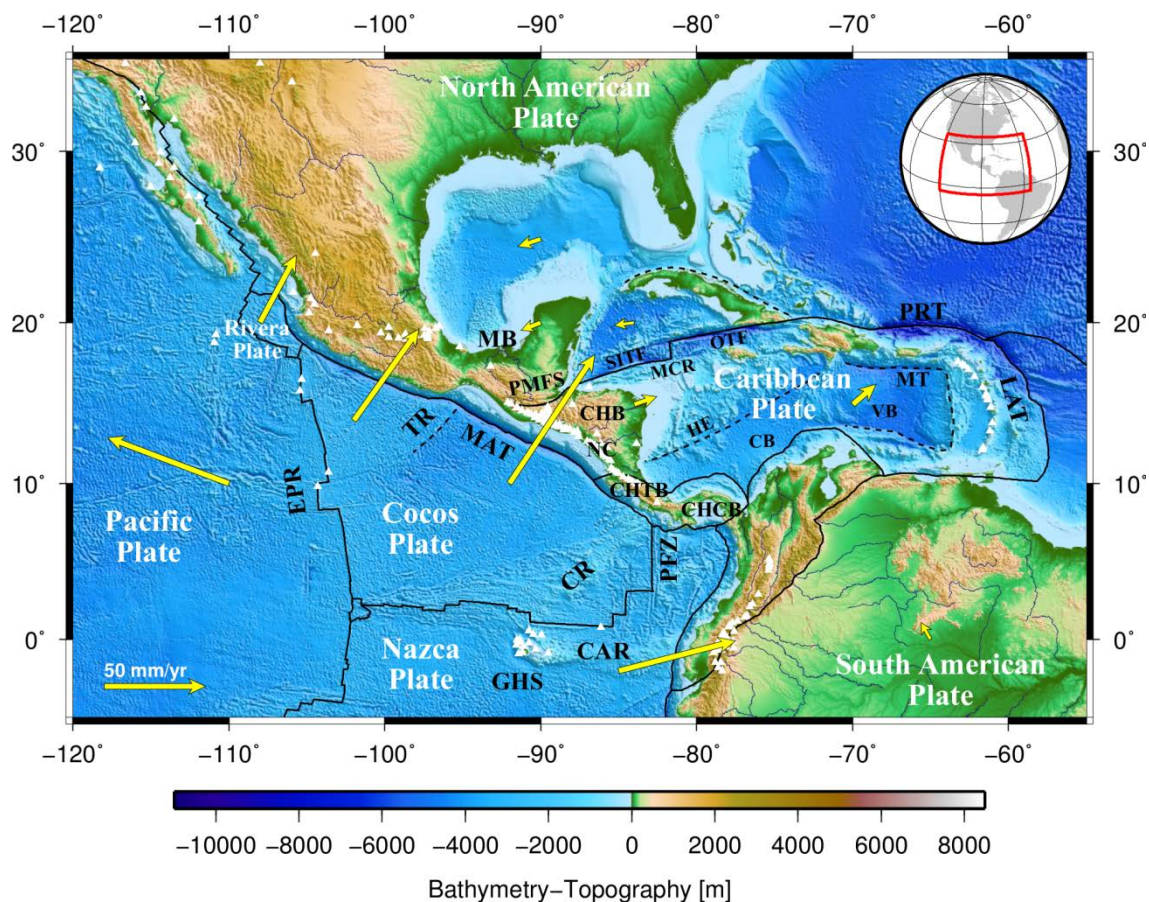
**Figure 1.** Geotectonic setting of Central America and surrounding regions. Shaded

relief image of bathymetry and topography is from ETOPO1 digital data (Amante and

Eakins, 2009), and boundaries of lithospheric plates are based on the PB2002 model

(Bird, 2003). Yellow arrows denote vectors of the plate motion from the MORVEL

model (DeMets et al., 2010) with respect to the NNR reference frame as calculated at

the given position with the Plate Motion Calculator

(http://www.unavco.org/community_science/science-

support/crustal_motion/dxdt/model.html). Triangles show the position of Holocene

volcanoes (Siebert and Simkin, 2002). Abbreviations: CAR, Carnegie Ridge; CB,

Colombian Basin; CHB, Chortis Block; CHCB, Chocó Block; CHTB, Chorotega Block;

CR, Cocos Ridge; EPR, East Pacific Rise; GHS, Galápagos Hotspot; HE, Hess

Escarpment; LAT, Lesser Antilles Trench; MAT, Middle America Trench; MB, Maya

1    Block; MCR, Mid-Cayman Rise; MT, Muertos Trough; ND, Nicaraguan Depression;

2    OTF, Oriente Transform Fault; PFZ, Panamá Fracture Zone; PMFS, Polochic-Motagua

3    Fault System; PRT, Puerto Rico Trench; SITF, Swan Island Transform Fault; TR,

4    Tehuantepec Ridge; VB, Venezuelan Basin.

5
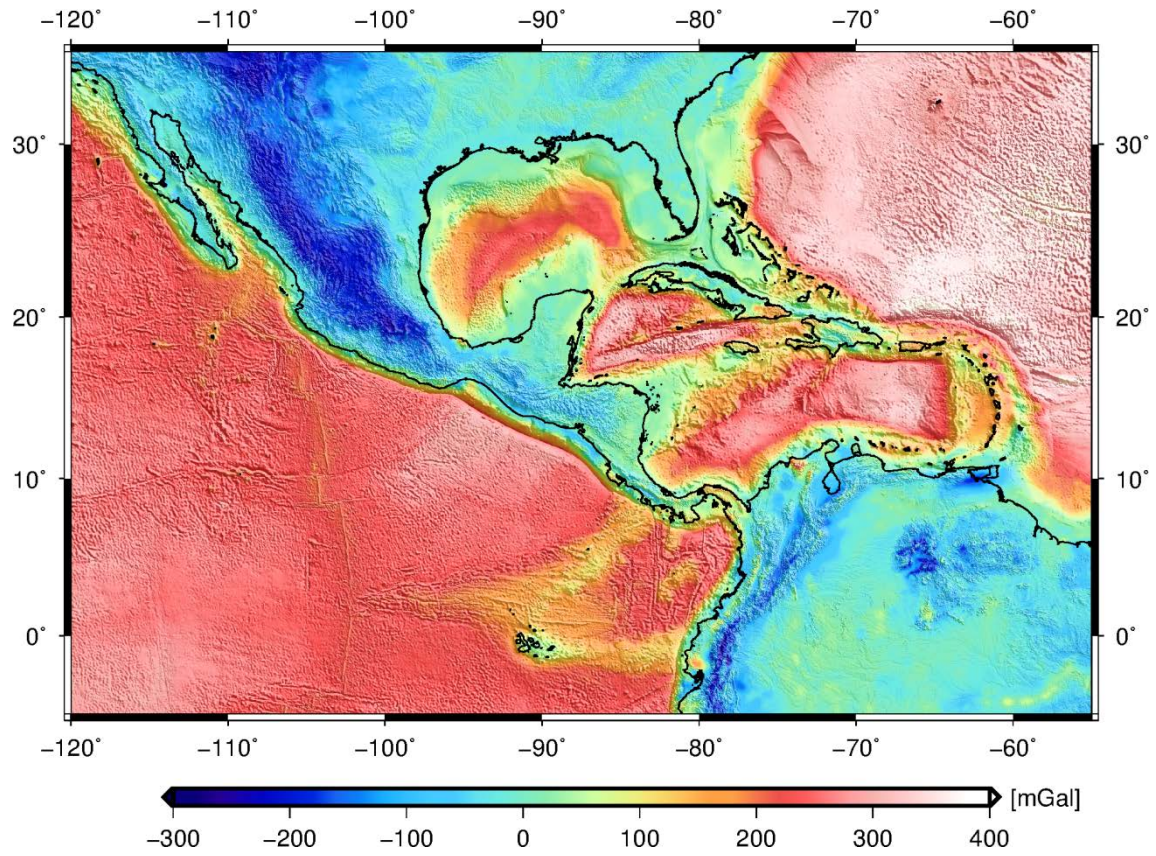
**Figure 2.** Bouguer gravity anomaly used for the analysis. Topography shaded relief superimposed.
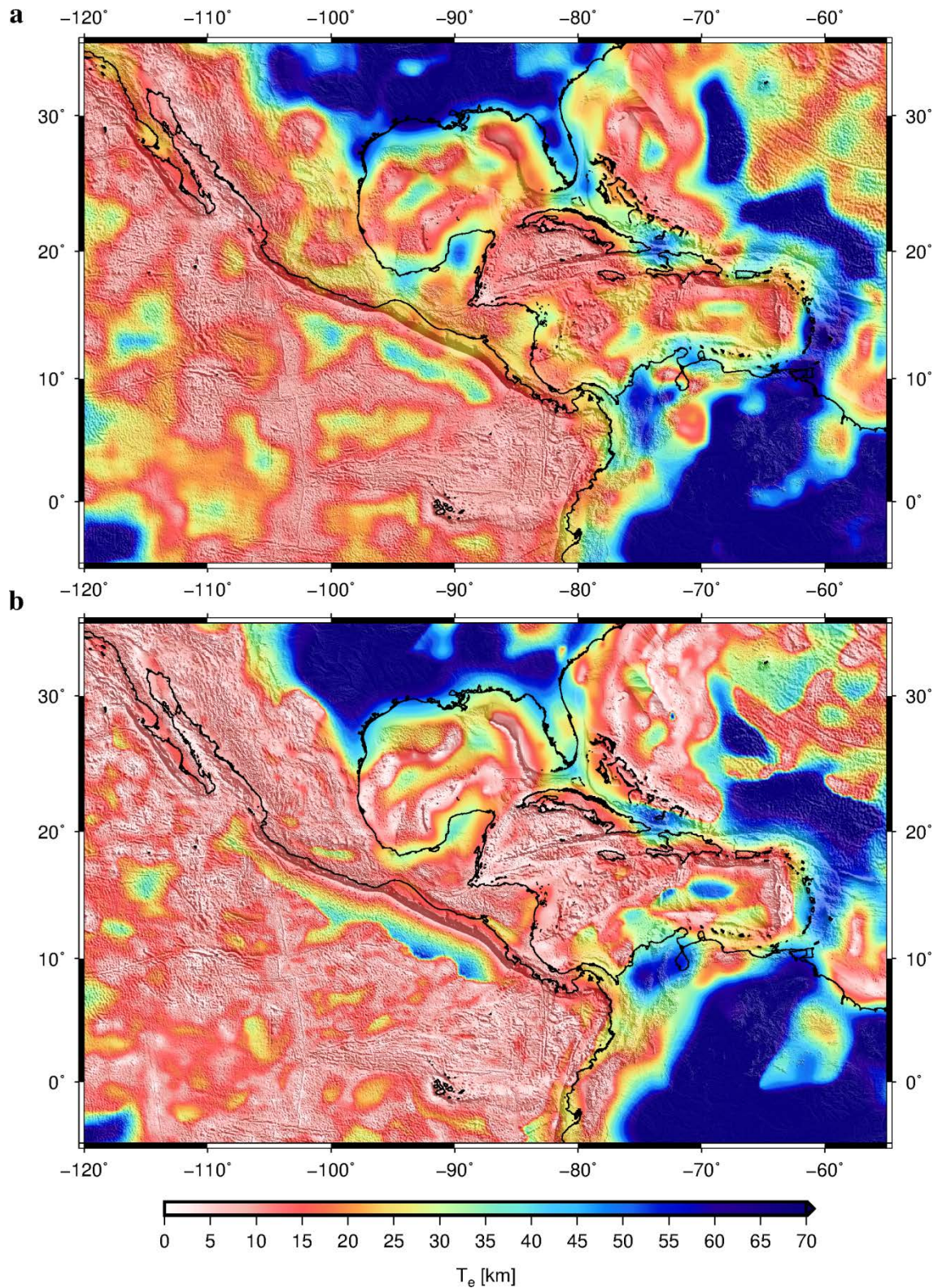
**Figure 3.** Effective elastic thickness, $T_e$, over Central America and surrounding regions from: (a) multitaper method, and (b) wavelet method. In both images, topography

1    shaded relief is superimposed. Fig. 3a shows final $T_e$ after merging the results from the

2    three different window sizes (see Section 2 and Supp. Fig. 1). The final $T_e$ structure

3    retains the primary characteristics of the largest window, but it better resolves the sharp

4    gradient between low and high $T_e$ areas and the short wavelength variations in $T_e$. Fig.

5    3b shows $T_e$ estimated from the wavelet method with $|\mathbf{k}_0|=2.668$.

6
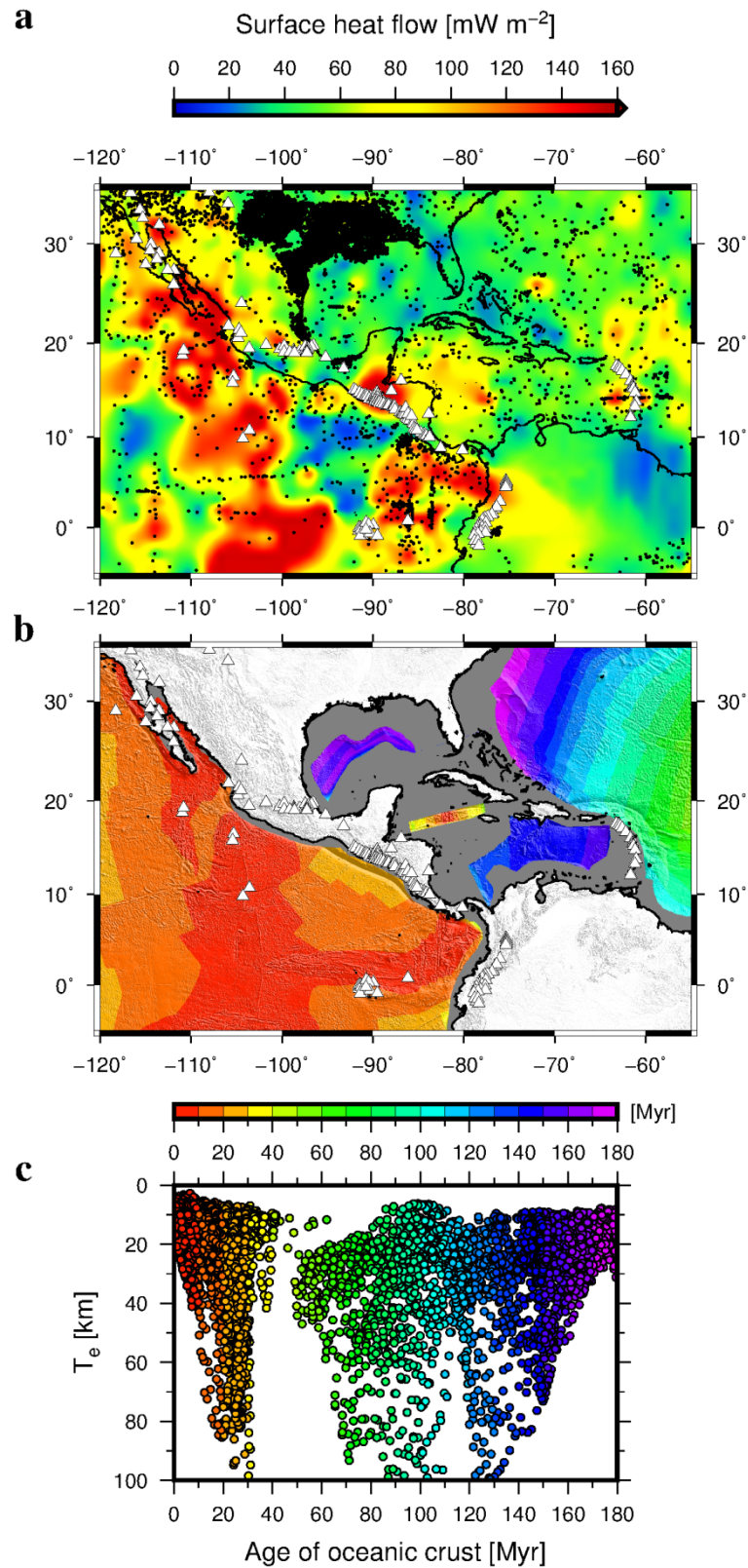
**Figure 4.** (a) Regional surface heat flow from the updated global heat flow database of the International Heat Flow Commission (Hasterok, 2010). Black circles indicate

1 measurement sites. White triangles show the position of Holocene volcanoes (Siebert

2 and Simkin, 2002). (b) Age-area distribution of ocean floor from Müller et al. (2008).

3 (c) Effective elastic thickness, $T_e$, from the multitaper method versus age of the oceanic

4 crust (Müller et al., 2008).

5
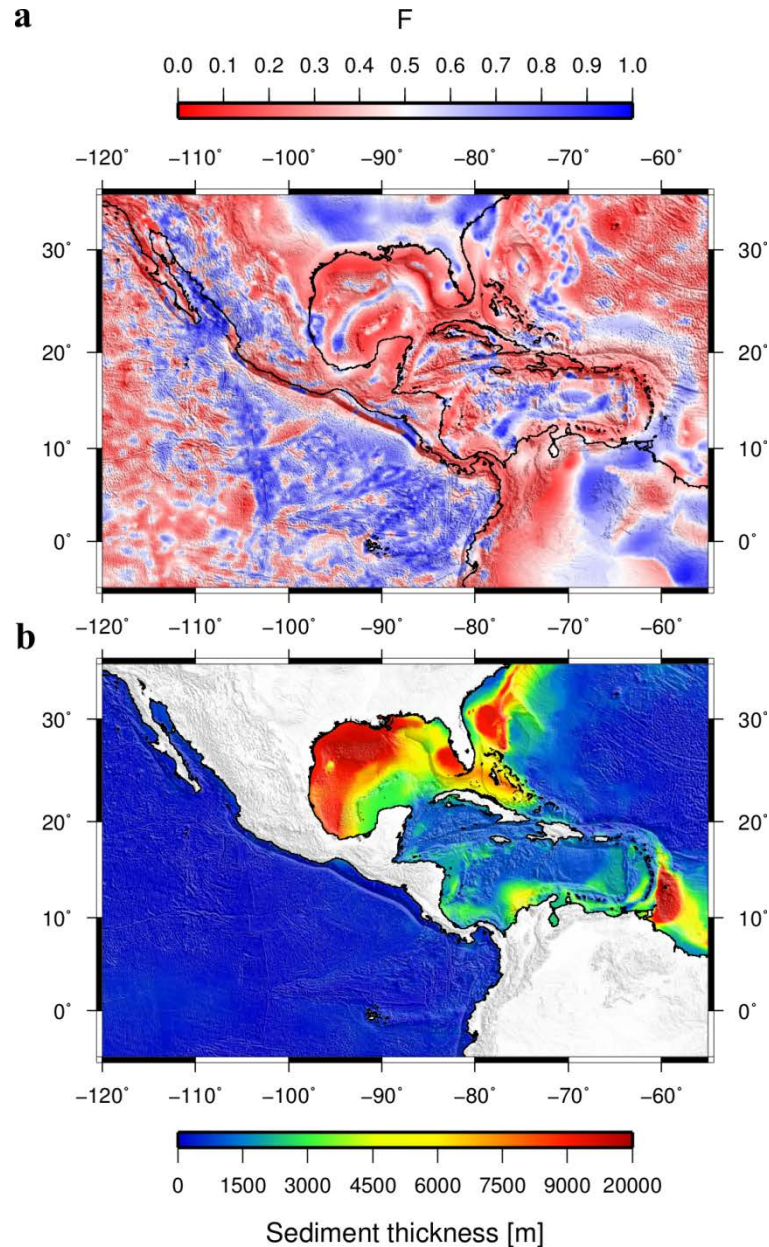
**Figure 5.** (a) Loading ratio ($F$) corresponding to the $T_e$ obtained from the wavelet method (Fig. 3b). (b) Sediment thickness (metres) on the seafloor in the study area from the 5 arc-minute digital total-sediment-thickness database for the world's oceans and marginal seas (Divins, 2003; Whittaker et al., 2013).
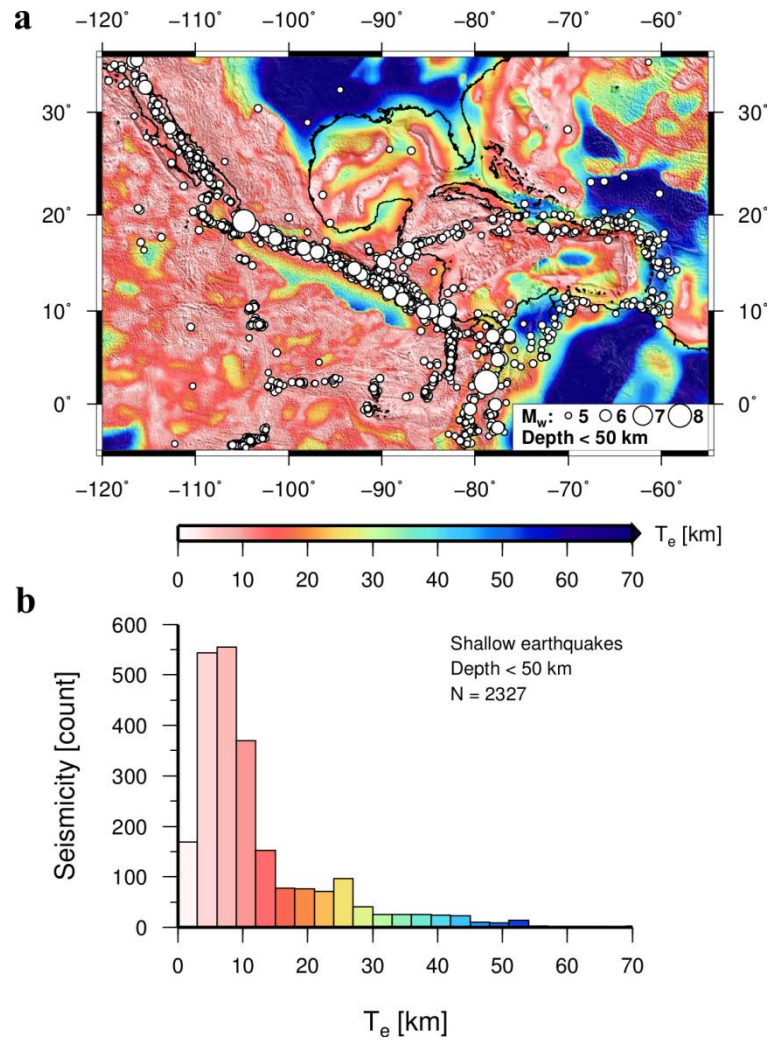
**Figure 6.** (a) Correlation between distribution of the shallow seismicity (depth < 50 km) from the Global CMT seismic catalog (Ekström et al., 2012) with $T_e$ derived from the wavelet method. (b) Histogram shows shallow earthquake events versus $T_e$.